AIAA 2011-3418

# Direct simulations of periodic roughness elements in a Mach 7 turbulent boundary layer

Izaak B. Beekman[*], M. Pino Martín[†]

**In this paper we discuss the direct numerical simulation (DNS) of a Mach 7.2 turbulent boundary layer over two dimensional square bar roughness elements. The boundary layer edge conditions and roughness configuration is chosen to match the experiments being performed in the Mach 8 wind tunnel at the Princeton University Gas Dynamics Lab.[1–4] Here, we present a discussion of the DNS technique and preliminary results. This discussion includes details of the simulation–such as computational mesh generation, flow initialization, numerical method, and boundary treatments–as well as a qualitative discussion of the underlying physics and the challenges they pose to numerical simulation.**

## I. Introduction

Very little detailed data exists on the effect of surface roughness on high-speed, turbulent boundary layers, yet flows of engineering interest are almost always over non-smooth vehicle surfaces. Such surfaces may be ablative or ceramic thermal protection systems, machined metal components, or external vehicle surfaces with rivets, fasteners, or tiles.

Despite the simplicity of geometrically-regular, periodic, rough, zero-pressure-gradient hypersonic boundary layer configurations, very few detailed studies have been performed on this flow to date. Two examples are the experimental studies mentioned above.[1,2] Additionally, a similar study and an in-depth description and assessment of the experimental PIV techniques used by Sahoo and coworkers is given in Schultze's thesis.[3] Other studies include that of Berg (1977), which provides measurements of mean and fluctuating quantities corresponding to sudden changes in surface roughness at Mach 6 over an adiabatic wall,[5] and Ekoto *et al.*[6,7] who investigate large-scale, periodic roughness (a roughness height of about 100 inner units) in a Mach 2.86, $Re_\theta \approx 60,000$, adiabatic-wall boundary layer with diamond mesh and square block roughness elements.

In this paper, we present the DNS data of a Mach 7.2 turbulent boundary layer temporally developing over spanwise aligned square bar roughness elements. The flow configuration is described in § II in terms of physical parameters and computational domain. Next, the numerical method and boundary treatments are presented in § III and the details of the grid and grid generation are covered in § IV. The initialization procedure and initial condition are discussed in § V. A comparison of the two initialization techniques, and a qualitative discussion of the physics is presented in § VI, and, finally, we draw conclusions and discuss challenges and future efforts in § VII.

## II. Flow configuration

The flow configuration considered in the present work is a temporally developing, zero pressure-gradient turbulent boundary layer over flat plate with square-bar roughness elements at Mach 7.2. The roughness element height, $k$, and width is 0.75 mm, and the roughness element pitch, $P$, is 6.25 mm. Figure 1 compares the geometry used in the simulations to the geometry used in the experiments at the Princeton University Gas Dynamics Lab. The primary difference is the smoothing of the roughness elements for the simulations, especially in regions of concave curvature. This is required to ensure the stability of the finite difference based

*Graduate Student, Department of Mechanical and Aerospace Engineering, Princeton University. Visiting Graduate Student, Department of Aerospace Engineering, University of Maryland, College Park.

†AIAA Associate Fellow. Associate Professor, Department of Aerospace Engineering, University of Maryland, College Park.

WENO scheme and avoid singularities in the mesh. The full extent of the computational domain is given in Figure 2. Here, the dimensions are normalized by the initial boundary layer thickness, $\delta_0$, as measured from the roughness element tops. This thickness is taken as the location where the mean velocity profile is 99% of the edge velocity, $U_e$. Further details of the initialization procedure are discussed in § V. The domain shown here is an acceptable size in the streamwise and spanwise directions to reduce spurious two point correlations–caused by the imposed periodicity–to zero within the domain for the initial flow. However, it has yet to be determined whether the modification of the turbulence structure due to the presence of roughness elements, or the growth of turbulence structures from the roughness elements and spatio-temporal evolution of the boundary layer will violate this requirement for the current domain size.

The wall and edge conditions are specified as follows. At the wall, a no-slip, isothermal boundary condition is used. The prescribed wall temperature is 352 K, which is within the 2% experimental error reported by Sahoo & coworkers.[1] This is roughly half of the recovery temperature for the given conditions. The usual kinematic no-slip and no-penetration conditions are applied at the wall as well. Away from the boundary layer, the edge velocity is 1174 m/s which, again, differs by only 2% from the reported experimental values. The edge Mach number is 7.16, the edge temperature is 66.9 K and the edge static pressure is 1418 Pa. These parameters are summarized in table 1.

| | $T_w$ (K) | $T_r$ (K) | $T_e$ (K) | $M_e$ | $U_e$ (m/s) |
|---|---|---|---|---|---|
| Experiment | $360 \pm 2.0\%$ | 647 | 61.7 | $7.3 \pm 1.0\%$ | 1150 |
| Computation | 352 | 677 | 66.9 | 7.16 | 1174 |

**Table 1. Summary of experimental and computational wall and edge conditions.**

Since the flow is so cold, special care must be taken evaluating the molecular transport coefficients. As Roy & Blottner[8] point out, Sutherland's law is only valid to $\sim 100$ K, below which it deviates significantly from observed values. Here, we use Keyes' formulation which was created to fit low temperature data, and has been experimentally validated to temperatures higher than those encountered here.[9]

The top of our domain is treated as a supersonic exit, and periodicity is imposed in the streamwise and wall normal directions. This streamwise periodicity causes the boundary layer to develop temporally rather than spatially, and has previously been shown to be acceptable for flat-plate turbulent boundary layers by Xu and Martín,[10] and has been successfully employed across a range of Mach numbers and wall temperatures, by Martín[11] and Duan, Beekman & Martín.[12,13] Whether or not this is an acceptable treatment for rough walls has yet to be determined.

## III. Numerical method

The numerical scheme used here is described in detail by Wu & Martín.[14] This is a curvilinear version of the code used and validated by Martín[11,15] across multiple Mach numbers and wall temperature conditions. We use a 4th-order accurate, weighted essentially non-oscillatory (WENO) scheme, which has been linearly and non-linearly optimized.[14,16,17] The linear optimization process reduces the dissipation and dispersion in smooth regions by adding an additional candidate stencil and adjusting the optimal stencil weights, resulting in the linear portion of the scheme being symmetric and bandwidth resolving efficiency optimized. The scheme has additionally been non-linearly optimized with limiters to avoid engaging the adaptation mechanism in regions of smooth flow. The details of the nonlinear optimization are given in Wu & Martín[14] and Taylor, Wu & Martín.[17]

For smooth wall boundary layers, as well as moderate Mach number shock-boundary layer interactions, the stability of the numerical scheme near the wall is not of primary concern: Even with very low dissipation numerics, the required wall normal grid spacing puts sufficiently many points close to the wall that any points where special boundary treatments are used are well below the sonic line, and dominated by viscous, elliptic phenomena. With the introduction of sufficiently large roughness elements, at a sufficiently high Mach number this is no longer the case. The large distortions of the grid around the roughness element as well as the presence of strong convective and hyperbolic phenomena makes the stability of the simulation quite sensitive to the spatial discretization scheme near the wall, and the computational grid.

Two popular approaches to boundary treatments are as follows: In the first, the same spatial scheme is utilized everywhere, but the appropriate number of "ghost" cells at the wall must be specified to provide information across the entire spatial stencil, even at the wall. The second technique is to reduce the size of the spatial stencil near the wall, resulting in a reduction of local spatial order of accuracy. We choose to adopt the second approach since, specifying the a large number of ghost cell values is challenging, and the reduction of spatial accuracy near the wall may be overcome by locally adding more grid points.

By progressively reducing the order of accuracy of the WENO scheme from fourth order, symmetric, bandwidth optimized (SYM-BO) to first order upwind at the wall, combined with a suitable computational grid, we can obtain a stable simulation. This way, we need only specify the value at one point at the wall, and we use the highest order of accuracy scheme possible, up to fourth order, given the available stencil in the wall normal direction. Using this approach we are able to run the simulation at a CFL number of 0.6 without incident.

For the spatial discretization of the viscous fluxes, 4th-order accurate central differencing is used, and time-integration is performed with a 3rd-order accurate, low-storage, explicit Runge-Kutta algorithm first introduced by Williamson.[18] The flow is initialized following the method of Martín.[11]

## IV. Computational grid

Two different grid configurations were used which can be seen below in Figure 3. Both grids are generated using a Schwarz-Christoffel mapping, which maps a rectangle to an arbitrary polygon. This mapping has the advantage of being orthogonal and continuously differentiable away from the domain boundaries since it is conformal. Additionally, the solution to the Schwarz-Christoffel parameter problem can be computed on a single CPU in less than a minute. One draw back of this technique, however, is that this SC parameter problem is highly nonlinear and stiff, and will not converge for certain geometries. As a consequence, the lengths of each side of the polygon cannot be too disparate. For more details on Schwarz-Christoffel mapping see the book by Driscoll & Trefethen: *Schwarz-Christoffel Mapping*.[19]

Both configuration 1, on the left of Figure 3 and Configuration 2 on the right use the same SC mapping. The lower surface of the polygon which the image of the transformation is specified as a half period of the experimental roughness geometry and the top surface is a straight, horizontal, segment at the desired height of the computational domain. Then, using symmetry and periodicity the full streamwise, wall-normal grid can be constructed. The smoothing of the roughness elements is achieved by moving the first $\xi$ coordinate line a small distance away from the real axis in the pre-transform space. This also helps drive the Jacobian determinant of the transformation closer to unity throughout the computational domain.

Once the SC parameter problem has been solved we can easily map points back and forth between Cartesian space on a rectangular domain and physical space on our curvilinear domain. To control the wall normal and streamwise coordinate spacing we introduce 1-D stretching functions to map our computational coordinates to our pre-transform, intermediate, Cartesian domain. We then apply the SC mapping to transform into physical, curvilinear space.

In the streamwise, $\xi$, coordinate direction we specify a periodic stretching to cluster points near the roughness element corners. This stretching function is specified as a superposition of trigonometric functions. The effect of this stretching on grid spacing is shown in Figure 4 both in computational space (red, bottom axis) and intermediate Cartesian space (blue, top axis). The grid spacing is normalized by the viscous length scale, $z_\tau = 0.02$ mm, reported by Sahoo *et al.*[1] There are 1152 points along the $\xi$ coordinate direction. In the spanwise direction the grid is uniformly spaced, with 256 points.

Configurations 1 and 2 differ in the choice of stretching functions in the wall normal direction, as well as the number of grid points in this direction. Configuration 1 uses a geometric grid stretching function and 104 points in the wall-normal direction, whereas configuration 2 uses an interior stretching function first proposed by Vinokur,[20,21] with 220 points. Both stretching functions are plotted in computational and intermediate-Cartesian space in Figure 5. Both are very similar but Vinokur's interior stretching function contains an inflection point away from the wall, which is specified to correspond to the approximate location of the shear layer we expect to be shed from the roughness element tops. Additionally, the approximate position of the boundary layer edge (as determined by the experiments at Princeton) is plotted for reference.

The action of conformal mappings have two principal effects: isotropic rotation and amplification. Squares get mapped into squares which have been rotated through an angle, and whose area has been increased or decreased. The Jacobian determinant of the transformation is the amplification factor by which the area of a differential element has changed. In Figure 6 the action of the SC map is visualized. The color contours show (on a log scale) the change in differential area (or length since the mapping is isotropic). The angle through which the map has rotated the local coordinate system is given by the white, labeled contours. Since the

Jacobian determinant of the SC transformation is near unity everywhere away from the roughness element corners, the grid spacing in intermediate Cartesian space is a close approximation to the final grid spacing throughout much of the boundary layer. A total of 30,670,848 grid points are used in the first configuration, and 64,880,640 points are used in the second.

## V. Initialization procedure

Configurations 1 and 2 also differ in the initialization procedure. Both initial conditions are derived from a grid-converged DNS of a smooth, flat plate at matching edge conditions, and lower Reynolds number than the anticipated rough wall Reynolds number, $Re_\theta \approx 5500$. The Van Driest transformed mean velocity profile is shown in Figure 7(a) and agrees well with previous findings. The shift of the logarithmic region above the usual additive constant of 5.2 can be attributed to the cold wall. As demonstrated by Duan, Beekman & Martín,[13] the cold wall increases the organization of the near wall coherent structures and increases the wall shear stress. This is also consistent with the Reynolds analogy; increased heat transport to the wall results in increased momentum transport.

Figure 7(b) shows streamwise velocity fluctuation profiles. These are given normalized by the traditional inner velocity scale–the friction velocity, $u_\tau$–as well as Morkovin density scaling.[22] The black line represents the smooth, initial condition DNS, the red line a Mach 5 DNS with nearly matching wall-to-recovery temperature ratio, and the blue line a Mach 7, nearly adiabatic DNS. These other data sets are from Duan, Beekman & Martín[12, 13] and agree quite well when Morkovin scaling is used.

By starting with a physically relevant initial condition we hope to shorten any initialization transient, and reach a physically correct state without exceeding our target Reynolds number. To this end, we initialize both configurations by interpolating the smooth, flat-plate DNS onto the new grid. In doing so we translate the location of the smooth wall vertically so that it coincides with the tops of the roughness elements. In both configurations we filter away any free stream noise using the filter functions shown in Figure 8, but in the first configuration we also aggressively filter out the near wall turbulent fluctuations, whereas we leave them alone in the second configuration. Then, to prevent discontinuities, we can set the velocity to zero in regions below the tops of the roughness elements, and set the temperature to the wall temperature here as well. This can be seen streamwise, wall-normal contour plots of instantaneous local Mach number and temperature in Figure 9. For the first configuration, since there are no turbulent fluctuations at the top of the roughness elements, we simply set the pressure or density to the mean wall pressure or density and use the equation of state to solve for the remaining flow variable. In the second configuration, we use smoothly varying blending fluctuations to extrude the pressure fluctuations and the roughness element height, to the mean pressure at the new wall. This can also be observed in Figure 9.

## VI. Preliminary results

Some interesting qualitative insights may be drawn from these simulations, even though we have yet to perform grid convergence studies and a detailed analysis. Figure 10(a) shows numerical schlieren visualization, defined by Equation 1, of configuration 1 after 11.4 large-eddy-turnover timescales. In addition to the clear depiction of large, downstream-leaning eddies seen throughout the boundary layer, we observe an interesting wave pattern being setup by the roughness elements. If we let the simulation evolve further, to $40.1\delta_0/U_e$, as seen in Figure 10(b), this regular wave patter seems to disappear from instantaneous visualizations. Here instead we see the formation of what appear to be spatially and temporally localized shocks originating from the roughness element faces, and curious 'V' shaped wave patterns. The former feature can be seen at the $x/\delta_0 = 3.75$ streamwise location and the latter at $x/\delta_0 = 6.5$. The second configuration, as seen in Figure 10(c), having evolved for the same amount of time as the field shown in Figure 10(a), displays an even richer, more chaotic flow field than the first configuration does when evolved for four times longer. As in Figure 10(b) strong, localized shocks can be seen on the roughness element faces, as well as strong expansions radiating from their downstream, top corner. The same constant, $c_1$, in the definition of the numerical schlieren is used for all images.

$$NS = \exp\left(-c_1|\nabla\rho|\right) \tag{1}$$

Additionally, in Figure 11, which plots iso-surfaces of zero streamwise velocity, colored by wall normal height, an organic streamwise organization can be seen, which is reminiscent of the near-wall streaks of smooth, flat-plate boundary layers. The first images in this series correspond to the same instances and configuration as the previous series of numerical schlieren plots. As is evident in the first figure, the initialization procedure for configuration 1 has eliminated virtually all of the inner most turbulent fluctuations. Only a pseudo-laminar, spanwise correlated, weak flapping of the shear layer formed by the roughness elements can be seen. When allowed to further evolve, for about 30 more large-eddy-timescales a spanwise organization begins to reappear, with steamwise aligned streaks visible. The second configuration also, exhibits a streamwise streak pattern reminiscent of smooth wall boundary layers, suggesting that these are in fact physical, and not just a consequence of the initialization procedure.

Figure 12 shows contours of instantaneous local Mach number, and significant regions of the flow below the roughness element tops are (instantaneously) traveling with supersonic velocities. This figure corresponds to the same configuration and time instant as the numerical schlieren in Figure 10(c). The shocks on the roughness elements can be seen in both figures. Additionally, between $x/\delta_0 = 6.5$ and 7.5 there appear to be four transverse vortex heads arranged in a downstream leaning angle, suggesting the presence of a hairpin-vortex packet. These vortices can be seen rolling up in both the schlieren and Mach number contour images.

Combining streamwise velocity information from Figure 13 with the contours of instantaneous, local Mach number, Figure 12, we see some interesting features. First, there is a shear layer, which is suspended between roughness element tops which flaps significantly in the wall normal direction. Sometimes this shear layer is separated and above the roughness element tops, and other times, sweep events drive it well below the roughness element tops. In this case, if we carefully inspect the base of roughness elements which have just collided with fast moving eddies, we can see regions of reversed flow very near the wall, close to or above sonic velocities.

Also, if we observe the wall normal velocity fluctuations of the first configuration after about $10\delta_0/U_e$, in Figure 14,we can see some interesting features. In front of the roughness elements, and immediately behind them we see that there tend to be re-circulation bubbles, rotating with angular velocities in the positive y direction. Also, some high-speed fluid colliding with the front of the roughness element appears to go down into this region of reversed flow, and some goes over the top of the roughness element forming a local shock. On the back of the roughness element, the flow is swept downwards as it expands around the roughness element corner and trailing recirculation bubble. Additionally, the curious 'V' patterns noted in Figure 10(b) might be associated with some sort of local shock reflection or flow reattachment, judging by the discontinuities in wall normal velocity at these locations.

## VII. Conclusions, challenges and future work

Despite the qualitative, and somewhat informal nature of the present analysis, some interesting flow features have been observed for high Mach-number flow of square bar roughness elements. First, strong shear layers are shed from the roughness element tops. These tend to flap in the wall normal direction. When these shear layers are pushed towards the wall they can produce violent collisions roughness elements. These collisions result in shocks forming very near the roughness element surface, and often reflecting back upstream. Other strong compressibility effects may also be present near the wall, including shock reflections caused by flow reattaching between roughness elements or strong expansions off the downstream top corner of the roughness elements.

Despite the exotic configuration relative to a smooth wall, flat-plate boundary layer, some striking similarities between the two flows still appear to exist. For instance the flow appears to organize itself into regions of downstream-leaning coherent structures. These structures sometimes appear to have vortices embedded in them consistent with the incompressible hairpin-packet model of Kim & Adrian.[23] Additionally, despite removing all near wall turbulence in configuration 1, streamwise aligned streaks of alternating high and low momentum fluid appear to be present, and have a characteristic spanwise length which is of the same order of magnitude as smooth, incompressible flat-plate boundary layers.

These flow features, especially the strong compressibility effects observed very near the wall, pose a large challenge numerically. Robust, stable, shock-capturing boundary treatments are required, otherwise the simulation will become unstable and crash. The local grid spacing, and topology also couples with the near wall boundary treatment. Large turning angles caused by sharp roughness features exacerbate the stability problems, and an appropriate streamwise and wall normal grid spacing is required in these regions, both to resolve the fine scale flow features, and to ensure stability.

As we pursue this work and refine this study, we intend to investigate other grid generation techniques to provide computational grids with a more economic distribution of points. Also, we may perform spatially developing simulations of a turbulent boundary layer on a smooth flat plate, which transitions to roughness. Schlieren images from the experiments conducted at Princeton, seen below in Figure 15, indicate the presence of a regular wave pattern. It is possible that the initialization techniques presented here are insufficient to model the physics seen in the experiments; the quiescent initial condition might be too quiescent, and not recover from the initialization transient soon enough, and the more violent initialization condition might overshoot the Reynolds number. Or these schlieren images with such ordered wave patterns might be an artifact of the spanwise integration of the experimental schlieren technique.

## Acknowledgments

This work is sponsored by NASA under Grant NNX08AD04A and the Air Force Office of Scientific Research under grant AF/9550-09-1-0464. Computational resources provided by the University of Maryland CRoCCo Lab which is part of the UMD Aerospace department, and the University of Maryland Institute for Advanced Computer Studies (UMIACS). We also wish to acknowledge our collaborators at the Princeton University Gas Dynamics Lab, especially Alexander Smits, Dipankar Sahoo and Owen Williams.

## References

[1]Sahoo, D., Papageorge, M., and Smits, A. J., "PIV Experiments on a Rough-wall Hypersonic Turbulent Boundary Layer," *AIAA Paper No. 2010-4471*, June 2010.

[2]Sahoo, D., Schultze, M., and Smits, A. J., "Effects of Roughness on a Turbulent Boundary Layer in Hypersonic Flow," *AIAA Paper No. 2009-3678*, June 2009.

[3]Schultze, M., *Experiments on Roughness in Hypersonic Boundary Layers at a DNS Accessible Reynolds Number*, Master's thesis, Stuttgart University, Institute for Aerodynamics and Gasdynamics, Pfaffenwaldring 21, 70569 Stuttgart, Germany, 2009.

[4]Sahoo, D., Ringuette, M. J., and Smits, A. J., "Experimental investigation of a hypersonic turbulent boundary layer," *AIAA Paper 2009-0780*, 2009.

[5]Berg, D. E., *Surface roughness effects on the hypersonic turbulent boundary layer.*, Ph.D. thesis, California Institute of technology, Pasadena CA, 1977.

[6]Ekoto, I. W., Bowersox, R., Beutner, T., and Goss, L., "Supersonic boundary layers with periodic surface roughness," *AIAA Journal*, Vol. 46, No. 2, 2008, pp. 486–497.

[7]Ekoto, I. W., Bowersox, R. D. W., Beutner, T., and Goss, L., "Response of supersonic turbulent boundary layers to local and global mechanical distortions," *Journal of Fluid Mechanics*, Vol. 630, 2009, pp. 225–265.

[8]Roy, C. J. and Blottner, F. G., "Review and assessment of turbulence models for hypersonic flows," *Progress in Aerospace Sciences*, Vol. 42, No. 7-8, 2007, pp. 469–530, Cited By (since 1996): 12.

[9]Keyes, F., "A Summary of Viscosity and Heat-Conduction Data for He, A, $H_2$, $O_2$, $N_2$, CO, $CO_2$, $H_2O$, and Air," *Trans. ASME*, 1951, pp. 589–596.

[10]Xu, S. and Martín, M., "Assessment of Inflow Boundary Conditions for Compressible Turbulent Boundary Layers," *Physics of Fluids*, Vol. 16, No. 7, 2004, pp. 2623–2639.

[11]Martín, M. P., "Direct numerical simulation of hypersonic turbulent boundary layers. Part 1: Initialization and comparison with experiments," *J. Fluid Mech.*, Vol. 570, 2007, pp. 347–364.

[12]Duan, L., Beekman, I., and Martn, M. P., "Direct numerical simulation of hypersonic turbulent boundary layers. Part 3. Effect of Mach number," *Journal of Fluid Mechanics*, Vol. 672, 2011, pp. 245–267.

[13]Duan, L., Beekman, I., and Martn, M. P., "Direct numerical simulation of hypersonic turbulent boundary layers. Part 2. Effect of wall temperature," *Journal of Fluid Mechanics*, Vol. 655, 2010, pp. 419–445, Cited By (since 1996): 4.

[14]Wu, M. and Martín, M., "Direct Numerical Simulation of Shockwave and Turbulent Boundary Layer Interactions over a Compression Ramp," *AIAA J.*, Vol. 45, 2007, pp. 879–889.

[15]Martín, M. P., "DNS of hypersonic turbulent boundary layers," *AIAA Paper 2004-2337*, 2004.

[16]Martin, M. P., Taylor, E. M., Wu, M., and Weirs, V. G., "A Bandwidth-Optimized WENO Scheme for the Direct Numerical Simulation of Compressible Turbulence," *Journal of Computational Physics*, Vol. 220, 2006, pp. 270–289.

[17]Taylor, E. M., Wu, M., and Martin, M. P., "Optimization of Nonlinear Error Sources for Weighted Essentially Non-oscillatory Methods in Direct Numerical Simulations of Compressible Turbulence," *Journal of Computational Physics*, Vol. 223, 2006, pp. 384–397.

[18]Williamson, J. H., "Low-storage Runge-Kutta schemes," *Journal of Computational Physics*, Vol. 35, No. 1, 1980, pp. 48–56, Cited By (since 1996): 261.

[19]Driscoll, T. A. and Trefethen, L. N., *Schwarz-Christoffel Mapping*, Cambridge University Press, 2002.

[20]Vinokur, M., "On one-dimensional stretching functions for finite-difference calculations," *Journal of Computational Physics*, Vol. 50, No. 2, 1983, pp. 215–234, Cited By (since 1996): 85.

[21]Vinokur, M., "ON ONE-DIMENSIONAL STRETCHING FUNCTIONS FOR FINITE-DIFFERENCE CALCULATIONS." *NASA Contractor Reports*, , No. 3313, 1980.

[22]Smits, A. J. and Dussauge, J.-P., *Turbulent Shear Layers in Supersonic Flow*, Springer, 2nd ed., 2006.
[23]Kim, K. C. and Adrian, R. J., "Very large-scale motion in the outer layer," *Phys. Fluids*, Vol. 11, No. 2, 1999, pp. 417–422.

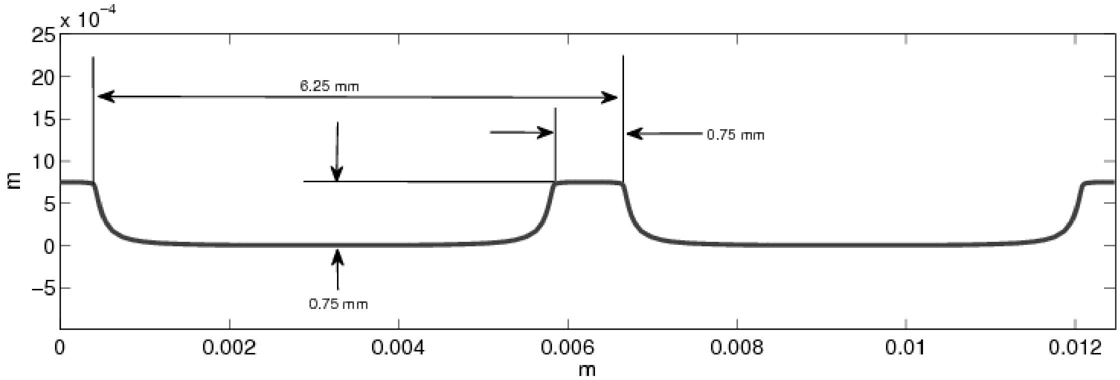


(a) Roughness geometry used for the simulations.

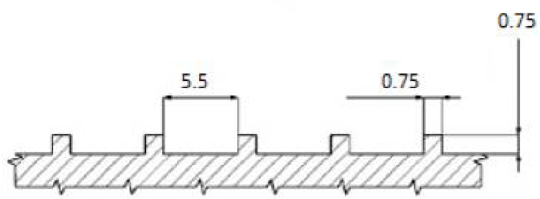


(b) Roughness geometry used in the experiments performed at Princeton University.[1] All dimensions are given in mm.

**Figure 1. Comparison of roughness geometries.**

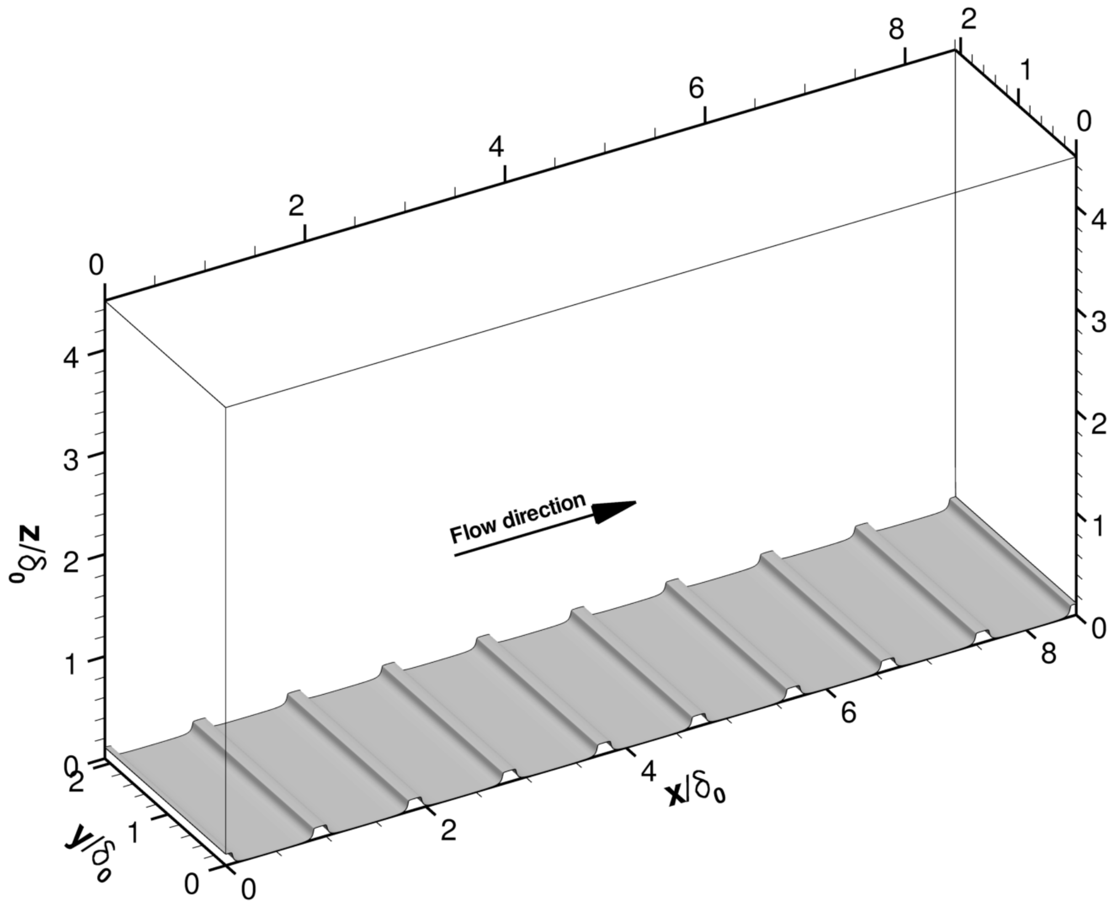


**Figure 2. A visualization of the computational domain. The wall is shown in gray and the dimensions of the computational box are normalized by the initial boundary layer thickness, $\delta_0 = 6.6$ mm.**

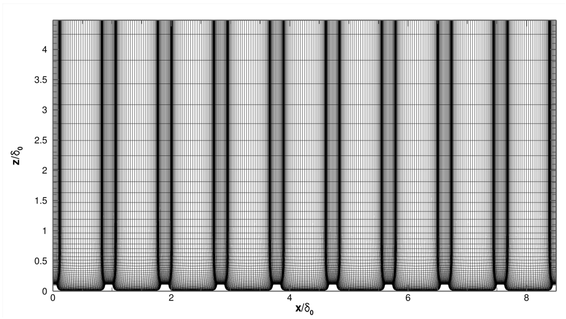


(a) The full computational mesh with every other point removed along the $\eta$ and $\xi$ computational coordinate lines. Geometric stretching is used in the wall normal direction.

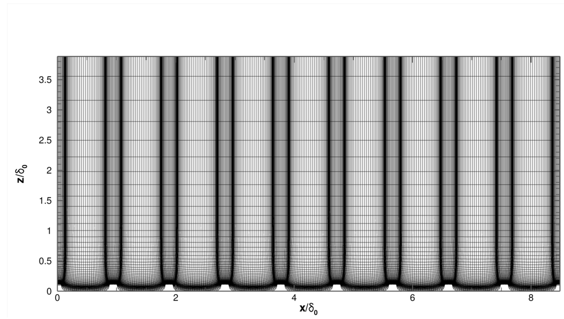


(b) The other full computational mesh with every other $\eta$ and every 3 out of 4 $\xi$ coordinate lines removed. The wall normal grid stretching is the interior grid stretching scheme proposed by Vinokur.[20]

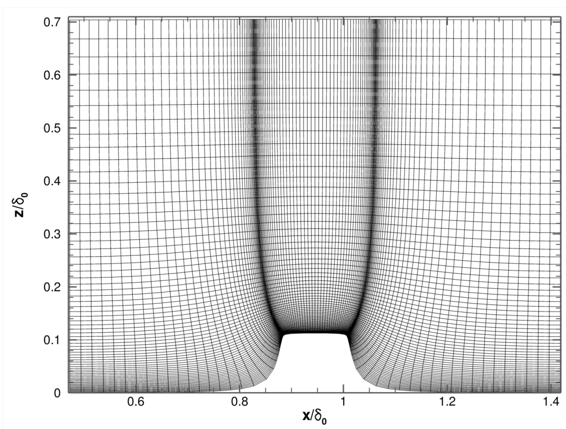


(c) A close up of a single roughness element. No grid points omitted, geometric wall normal stretching is used.

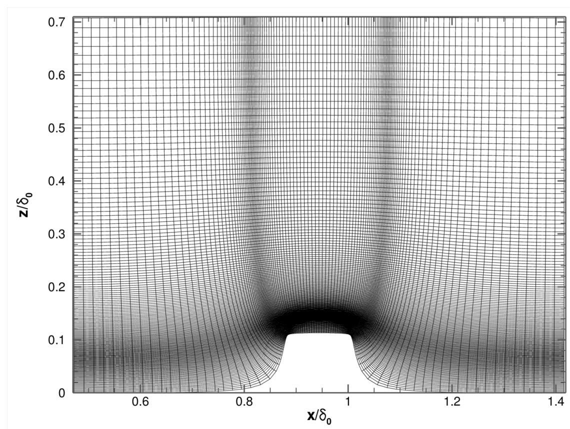


(d) A close up of a single roughness element. No grid points omitted, Vinokur's interior stretching scheme is used in the wall normal direction. Image aliasing and compression artifacts exaggerate the a very minor difference in the parameters of the streamwise stretching function.

**Figure 3. The computational mesh.**

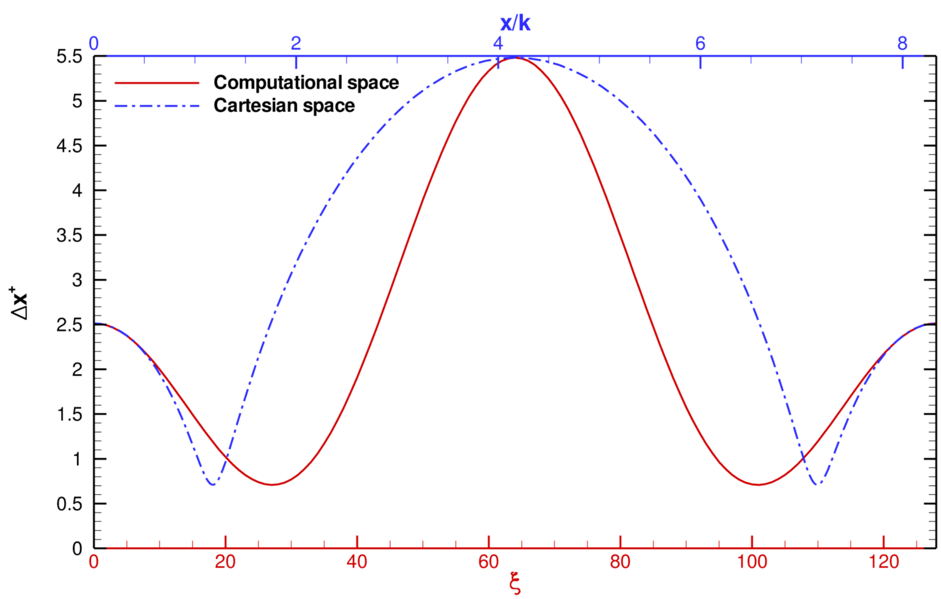


**Figure 4. Streamwise periodic grid stretching as a function of computational coordinate $\xi$ and intermediate Cartesian coordinate $x$ normalized by the roughness element height, $k$. Only one of the nine periods is shown here.**

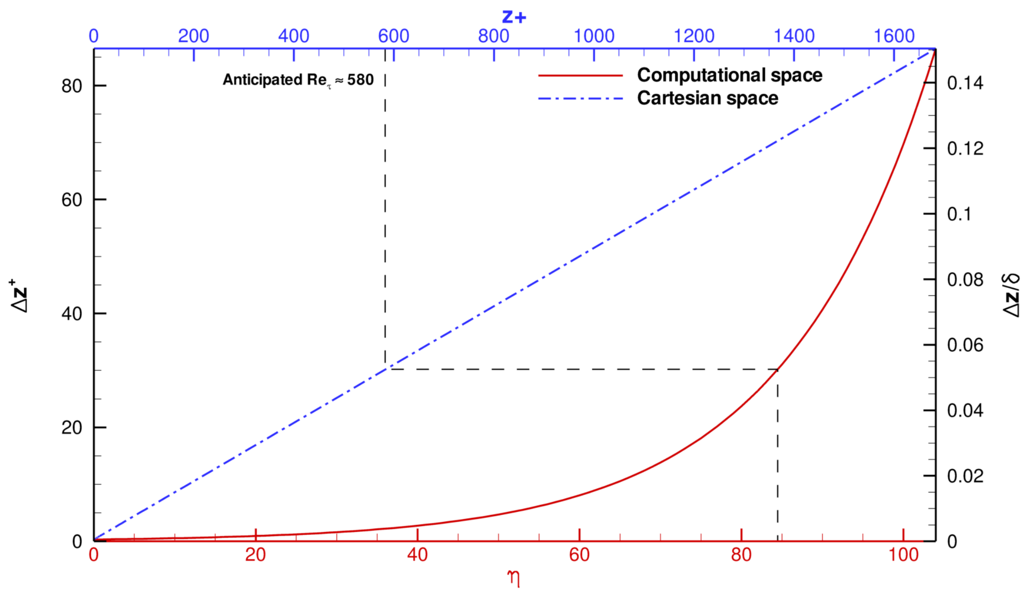


(a) Geometric stretching function: $Z_k = z_2(\alpha^{k-1} - 1)/(\alpha - 1)$

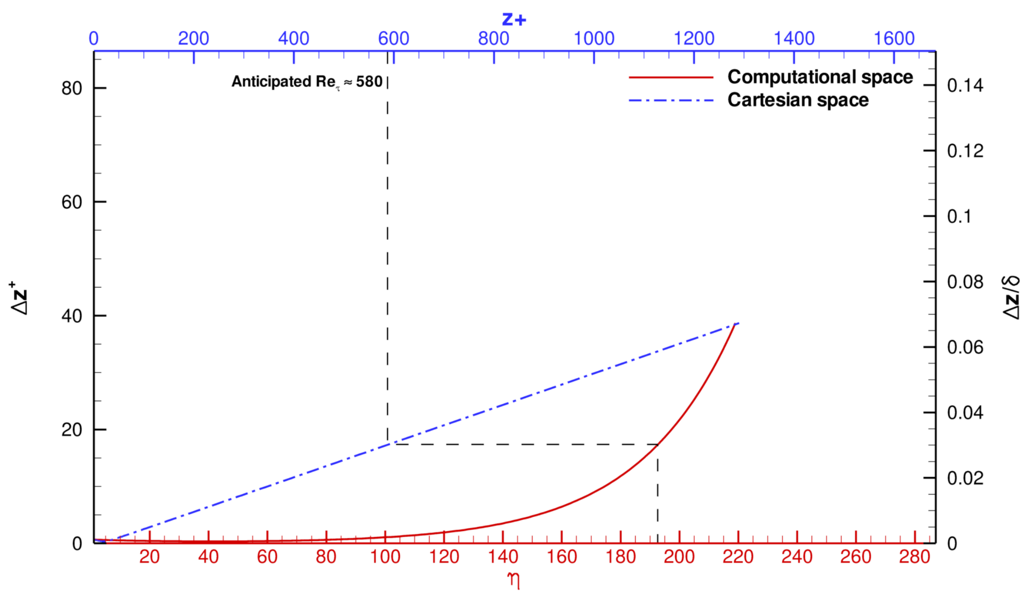


(b) Vinokur's interior stretching function

**Figure 5. Wall normal stretching as a function of computational coordinate $\eta$ and intermediate Cartesian coordinate $z$ normalized by the anticipated viscous length scale, $z_\tau$. The anticipated friction Reynolds number is also plotted for reference. Anticipated values are obtained from the experiments at Princeton University.**

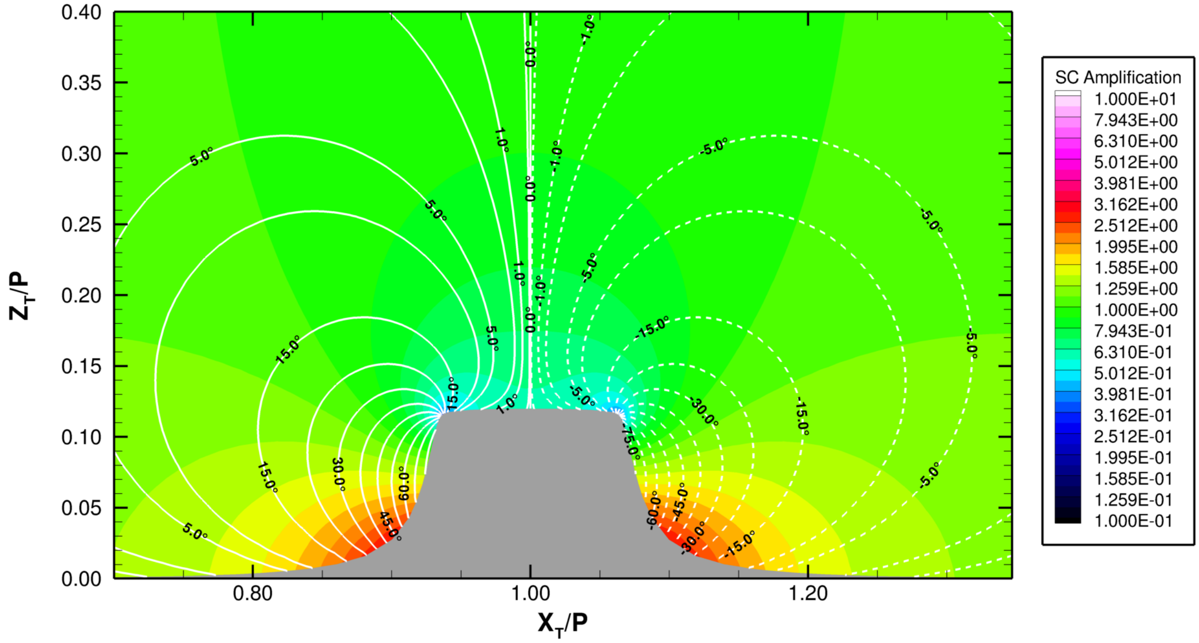


(a)

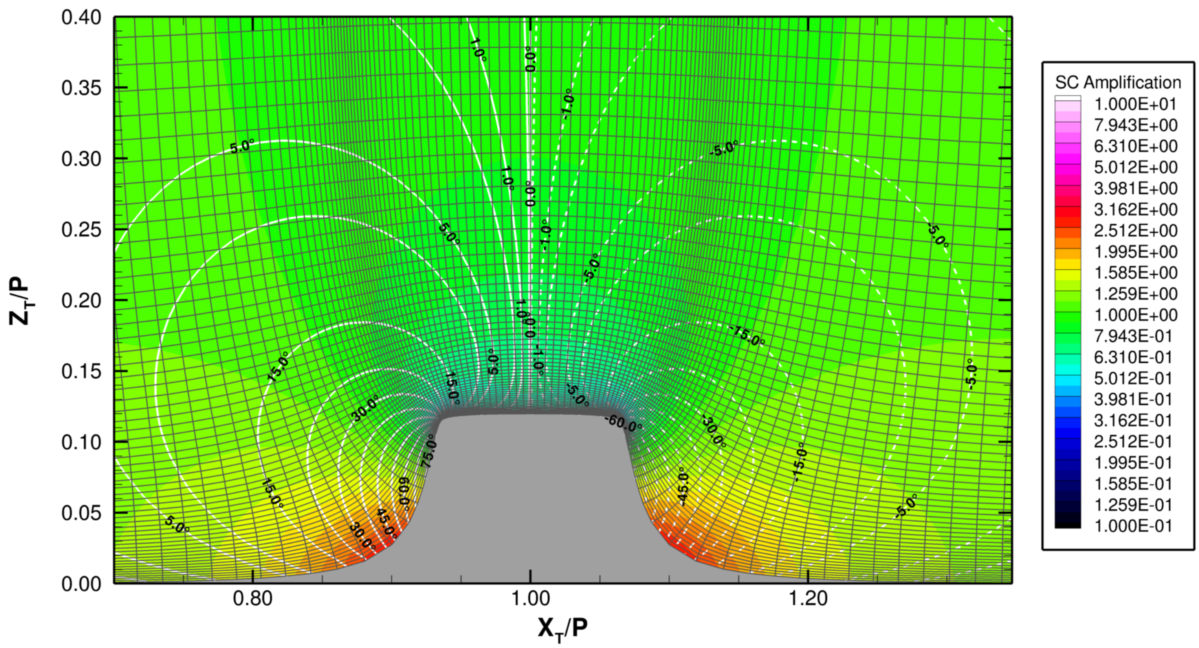


(b)

**Figure 6. A visualization of the action of the Schwarz-Christoffel transformation in mapping the intermediate Cartesian domain to physical coordinate space. The flooded contour levels show the degree of isotropic stretching, and equal the Jacobian determinant of the transformation. The white, labeled contour lines denote the the angle through which coordinate lines in intermediate Cartesian space are rotated by the transformation. Note the logarithmic color map, with 10 times amplification given as white, no amplification shown as green, and one tenth amplification flooded in black. For this geometry, the Jacobian determinant varies by approximately one decade from 0.3 to 3.**

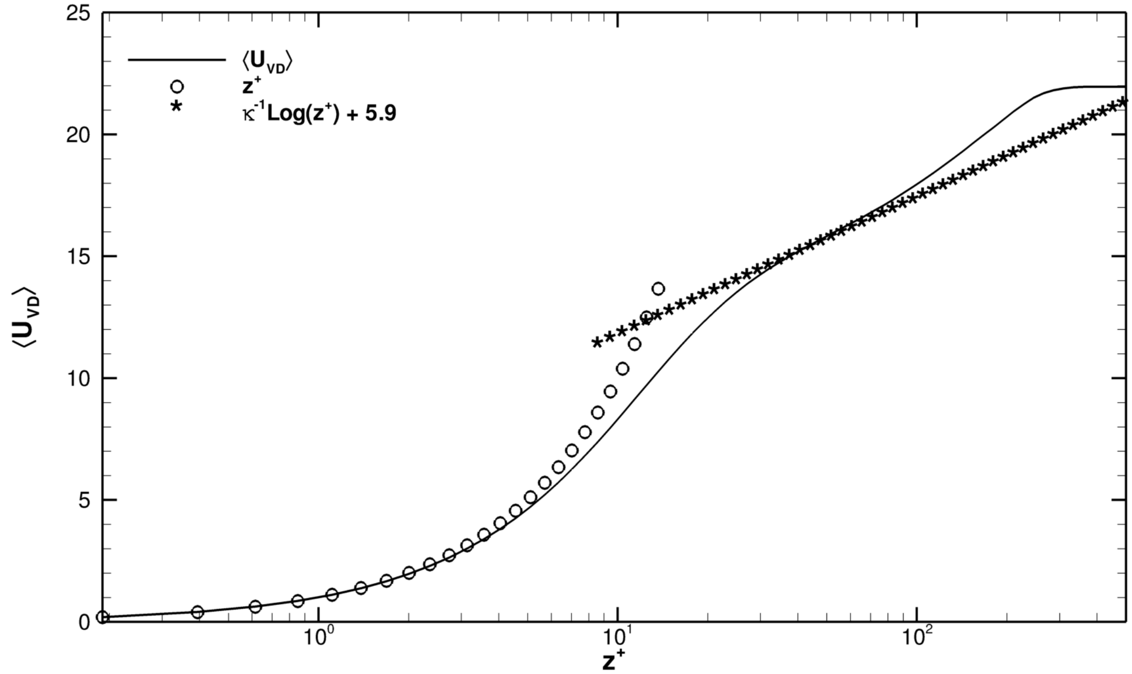


(a) The Van Driest transformed velocity profile of the smooth plate DNS from which the initial condition was derived. Here the Von Karman constant, $\kappa$, is taken as 0.41. The shift of the logarithmic region above the normal additive constant of $\sim 5.2$ is consistent with the Reynolds analogy: The cold wall increases the organization of the turbulence and the shear stress imparted on the wall as shown by Duan, Beekman & Martín.[13]

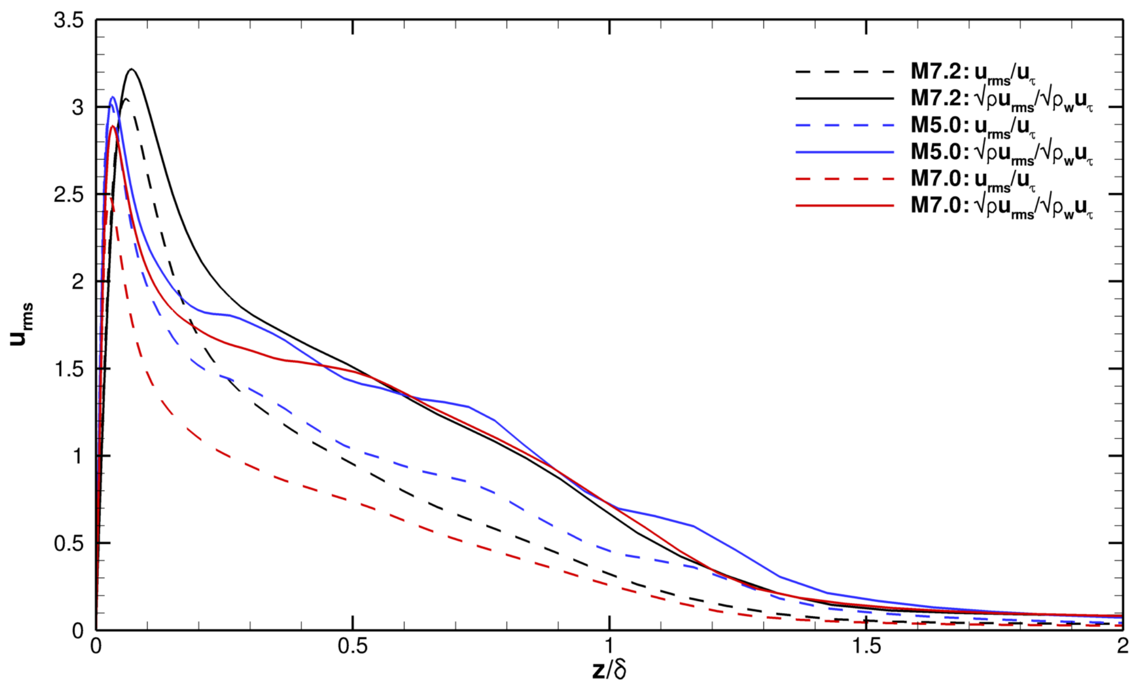


(b) Streamwise velocity fluctuations normalized with the friction velocity (dashed) and Morkovin[22] scaling (solid). The red lines are at nearly the same wall-to-recovery-temperature ratio but at Mach 5, and the blue lines are at Mach 7 for a nearly adiabatic wall. The Mach 5 and 7 data is the same as that given by Duan, Beekman & Martín 2010 and 2011 respectively.[12,13]

**Figure 7. Van Driest transformed velocity profile, and streamwise fluctuations of initial condition derived from a flat-plate DNS at matching edge conditions.**

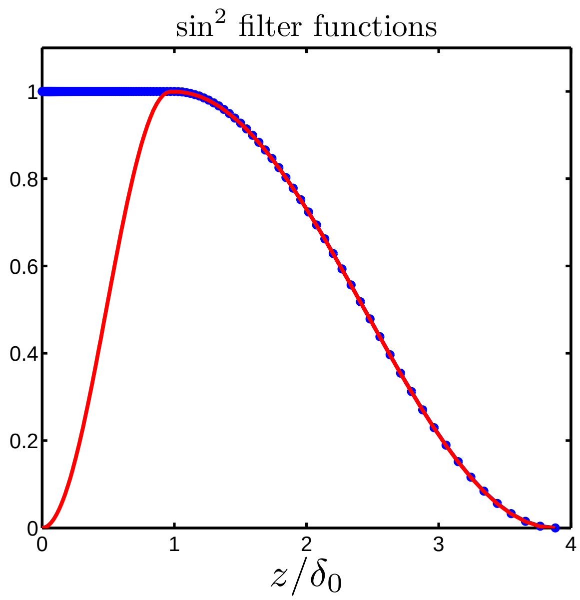


**Figure 8. Filter functions applied to the initial flow field. Blue: Filtering of free-stream fluctuations only. Red: Free-stream and near wall fluctuations removed.**

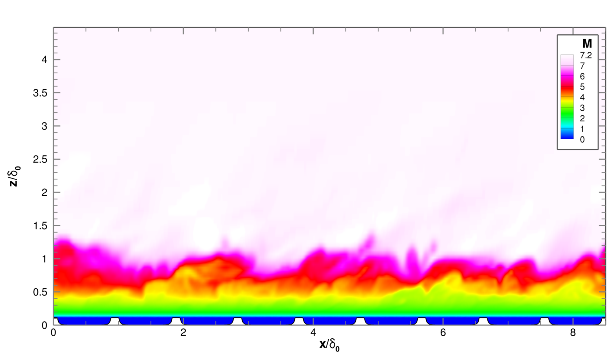


(a)

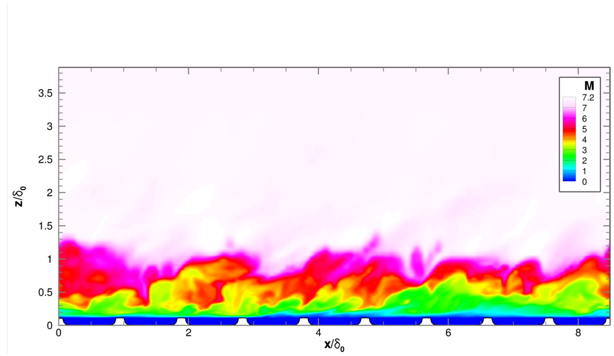


(b)

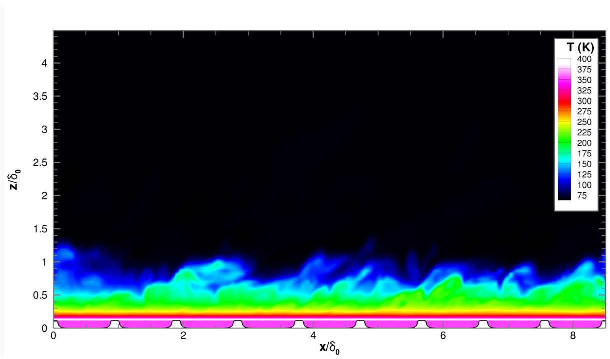


(c)

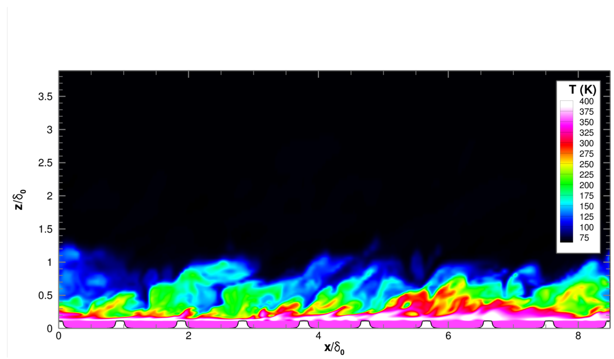


(d)

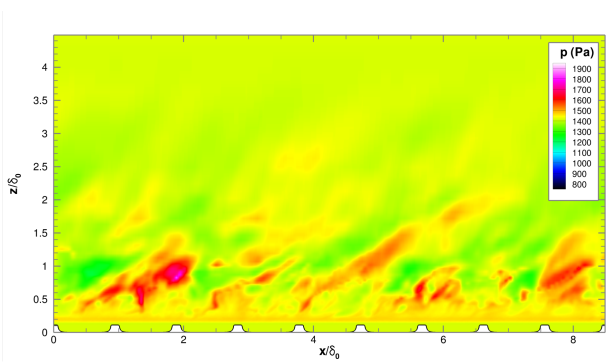


(e)

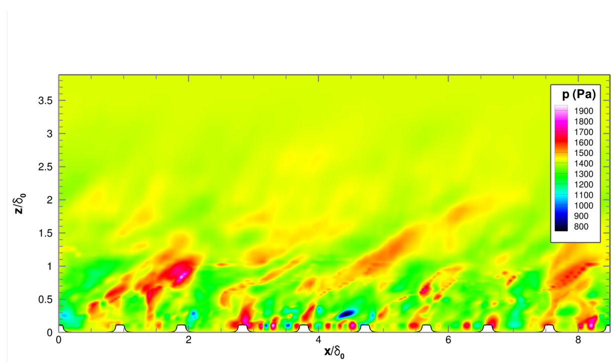


(f)

**Figure 9. Streamwise,wall-normal planes showing the two alternate initialization techniques. On the left, the near wall turbulent fluctuations have been removed using the blending function in Figure 8 whereas on the right the near wall fluctuations are retained. From top to bottom the figures show contours of instantaneous local Mach number, temperature and pressure. The top figures illustrate how the thermal and velocity no-slip condition is used to specify the flow in the inter-roughness-element regions, and the bottom most figures illustrate how the fluctuating flat plate wall pressure is smoothly blended from the roughness element height to the rough-wall surface.**

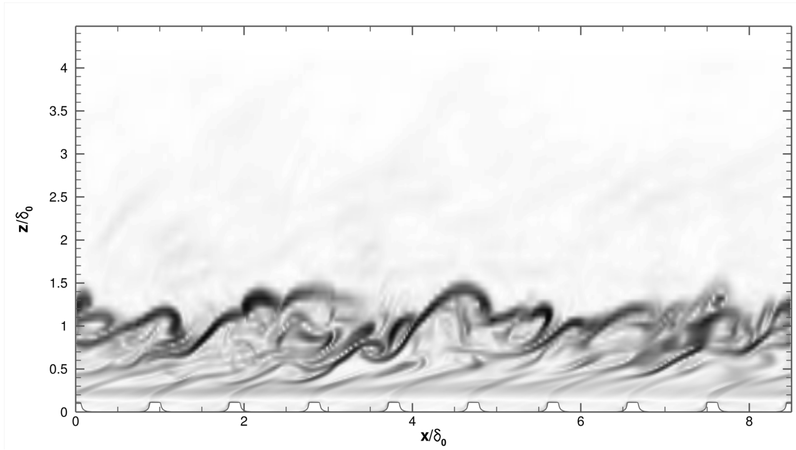


(a) Configuration 1 at $11.4\delta/U_e$

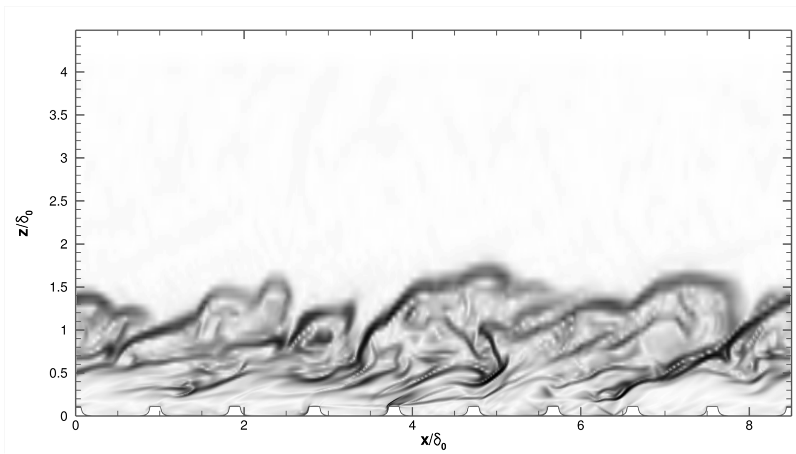


(b) Configuration 1 at $40.1\delta/U_e$

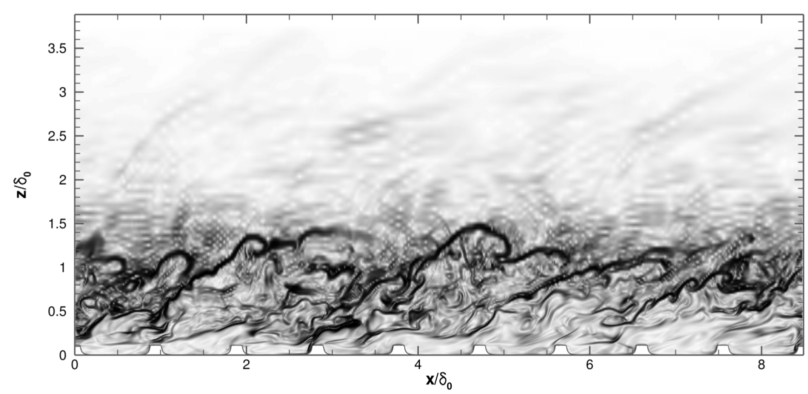


(c) Configuration 2 at $11.4\delta/U_e$

**Figure 10. Comparison of numerical schlieren images between configuration 1 and configuration 2 at different time instances.**

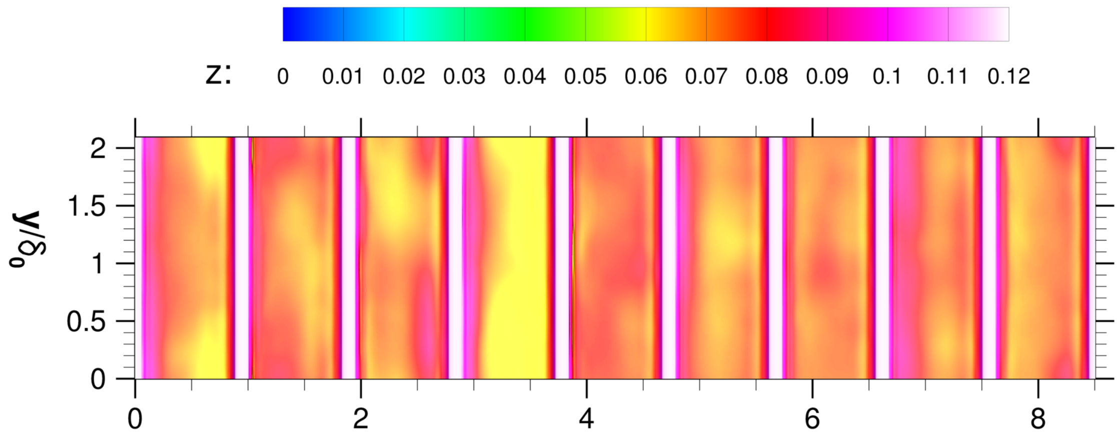


(a) Configuration 1 at $11.4\delta/U_e$

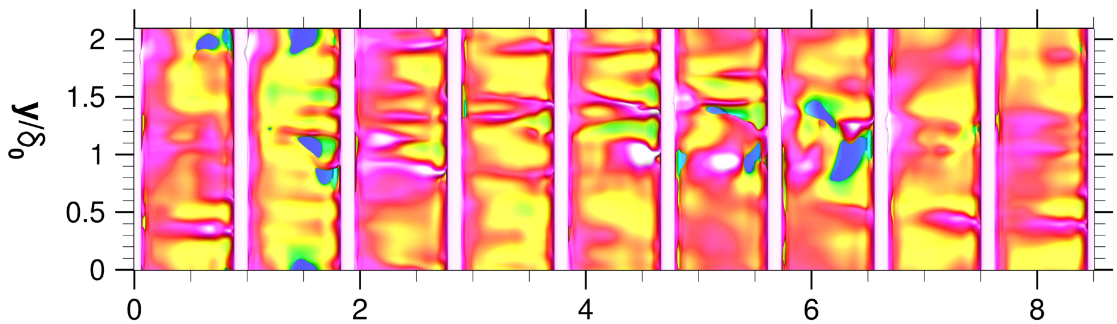


(b) Configuration 1 at $40.1\delta/U_e$

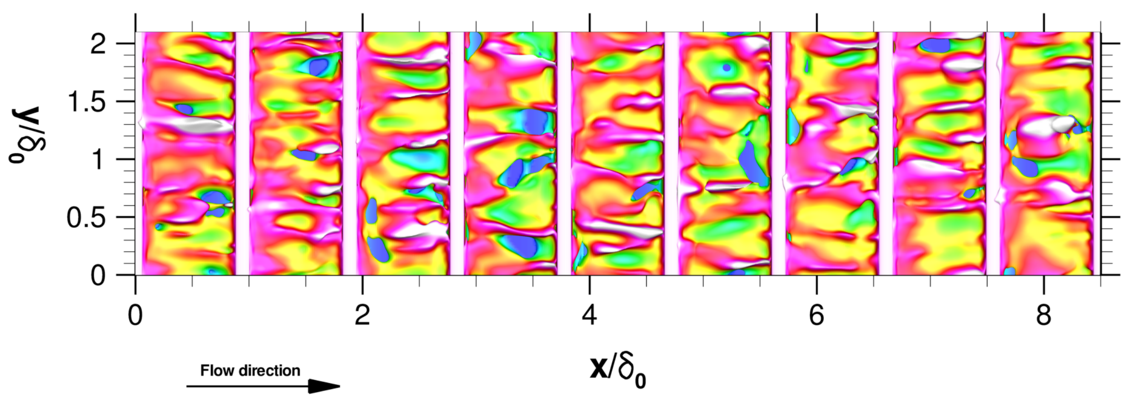


(c) Configuration 2 at $11.4\delta/U_e$

**Figure 11. Comparison of iso-surfaces of zero streamwise velocity (colored by wall normal distance) between configuration 1 and configuration 2 at different time instances.**

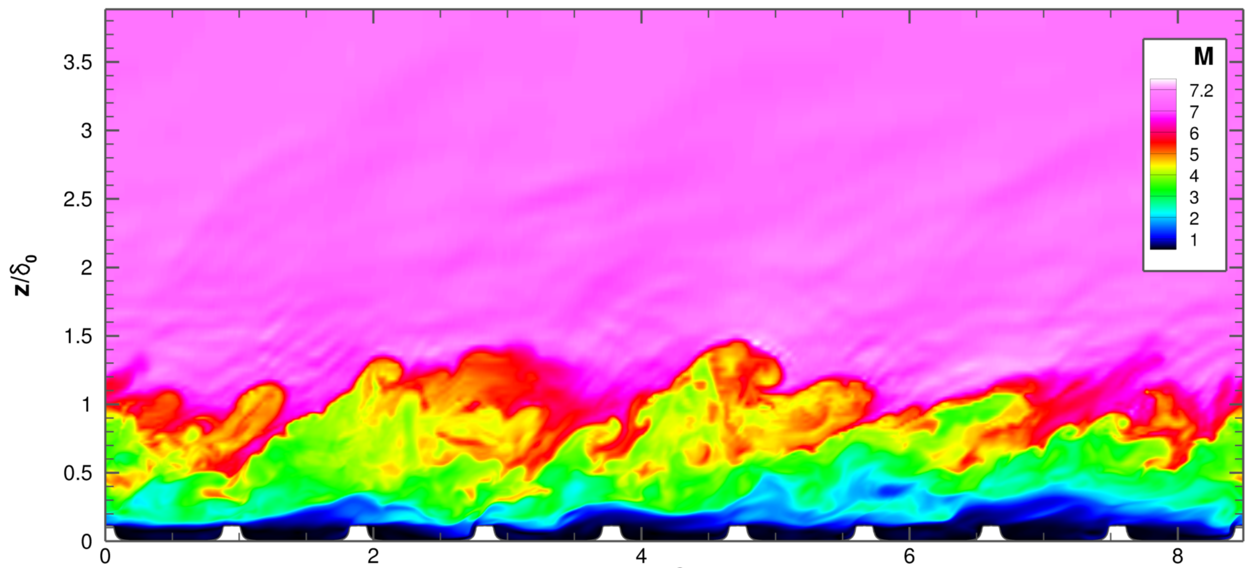


**Figure 12. Contours of instantaneous Mach number for configuration 2 at $11.4\delta/U_e$. Note the incursions of supersonic fluid below roughness element tops. Also, the plane appears to cut through a of set 4 or more spanwise aligned vortices arranged in a downstream leaning angle, reminiscent of a hairpin packet. These start at approximately $6.5x/\delta_0$ and end at $7.5x/\delta_0$, and can be seen where the contour level transitions from green to yellow. The roll up of these vortices is also evident in the numerical schlieren shown above taken at the same instant and spanwise location.**

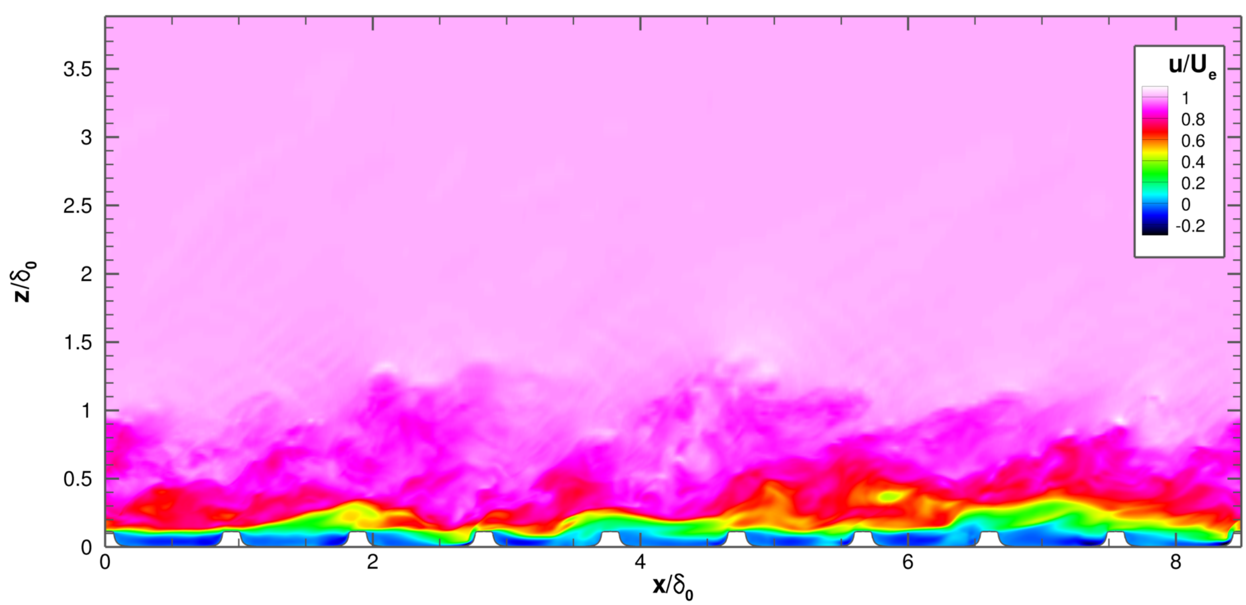


**Figure 13. Contours of streamwise velocity for configuration 2 at $11.4\delta/U_e$. The shear layer shedding from the tops of the roughness elements varies significantly in thickness, and meanders significantly. On the left, windward side of the domain the shear layer is quite compact in the wall normal direction and is flowing nearly straight downstream. It is not uncommon to see eddies with streamwise velocities greater than Mach 2 colliding with roughness elements. In fact, at the base of the rightmost roughness element, as a result of a particularly violent collision, there is a tongue of reversed flow with sonic velocity very near the wall.**

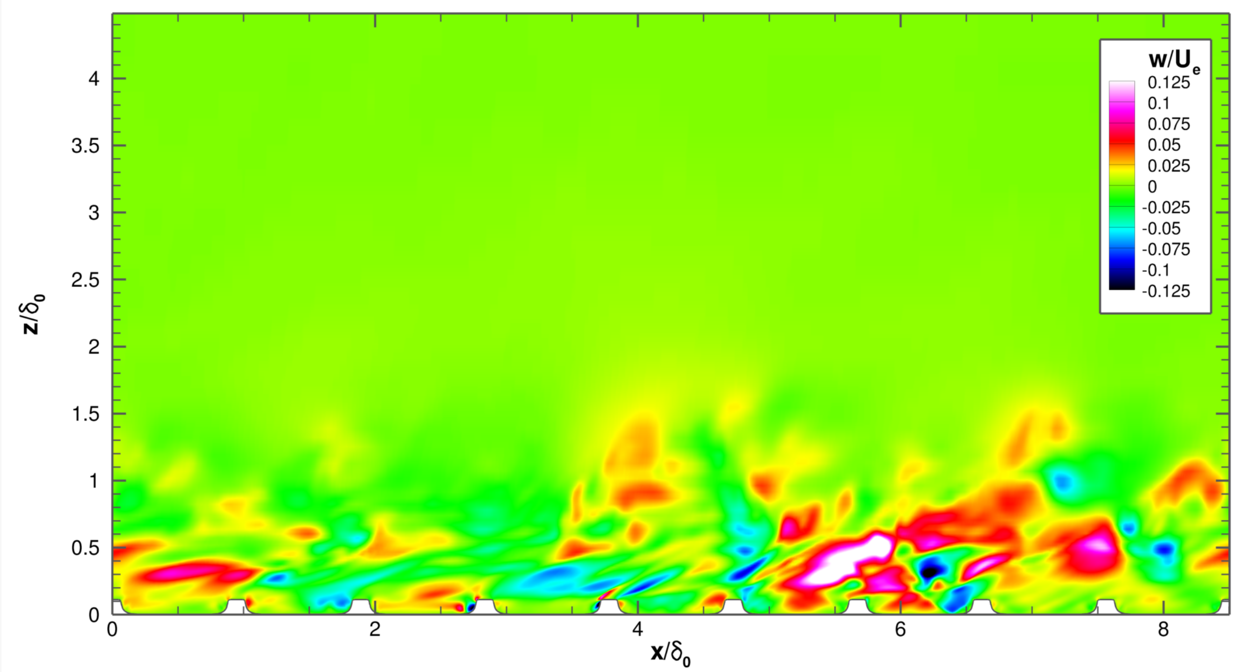


**Figure 14. Wall normal velocity contours for configuration 1 at $40.1\delta_0/U_e$. The flow field in the immediate vicinity of the roughness element centered at $3.75x/\delta_0$ exhibits a typical structure: A small recrculatig bubble of fluid can be seen on either side of the roughness element, both with positive spanwise vorticity as expected. The high velocity fluid impinging the front face of the element creates a shock wave which turns the fluid towards the free stream. Then, there is an expansion to realign the flow with top of the element. Finally, a small expansion fan turns the fluid behind the element back towards the wall.**

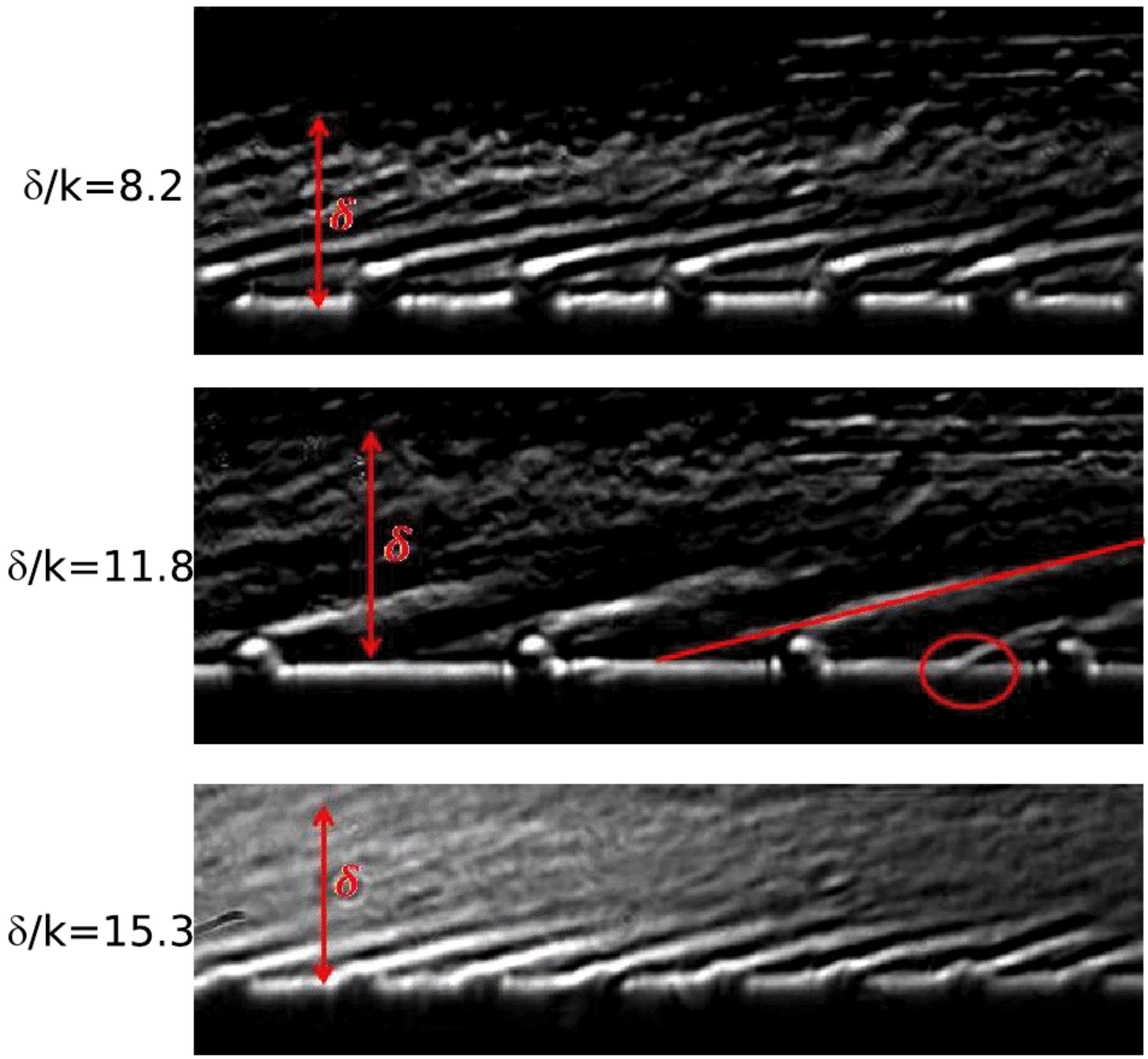


**Figure 15. Schlieren imagery of the experimental flow field with different roughness element heights. From private communication with Alexander Smits of Princeton University.**